ACCRETION DISKS AND ERUPTIVE PHENOMENA

SCOTT J. KENYON

Smithsonian Astrophysical Observatory

60 Garden Street, Cambridge, MA 02138 USA

1. Introduction

In the 1700's, Immanuel Kant and the Marquis de Laplace proposed that the solar system collapsed from a gaseous medium of roughly uniform density ([79], [105]). A flattened gaseous disk – the protosolar nebula – formed out of this cloud. The Sun contracted out of material at the center of the disk, while the planets condensed in the outer portions. Despite its simplicity, this model suffered from the *angular momentum problem* inherent to star formation: a cloud of gas and dust with the diameter of the solar system and the mass of the Sun has too much angular momentum to collapse to the Sun's present size. It took 150 years to solve this problem. C. von Weiszäcker worked out the basic physics of a viscous accretion disk, building on previous realizations that a turbulent viscosity could move material inwards and angular momentum outwards through the protosolar nebula ([178], [179]). With Lüst's steady-state solution ([119]), Kant's nebular hypothesis no longer suffered from the angular momentum problem and became the leading model for solar system formation.

Disk accretion is now known to power a wide range of astronomical sources. Starting with Kuiper's landmark study of β Lyr, viscous accretion disks have become central to our understanding of interacting binaries, where one star fills its inner Lagrangian surface and transfers matter into a disk surrounding a smaller companion ([103]). A disk surrounding a supermassive black hole is widely believed to drive the phenomena observed in active galactic nuclei (e.g., [175]). Accretion disks remain an important issue in star and planet formation, as described throughout this volume.

One striking feature of recent observations is the common phenomena observed in different accreting systems. All disks vary in brightness. These fluctuations range from rapid flickering on time scales as short as a few milliseconds up to long-lived eruptions with durations of decades or centuries.

Most accreting systems lose mass; practically all disks that lose mass eject material in a well-collimated jet ([115]). These common phenomena occur in systems with luminosities ranging from much less than 1 $L_\odot$ in some interacting binaries up to 10^{11} $L_\odot$ in active galactic nuclei.
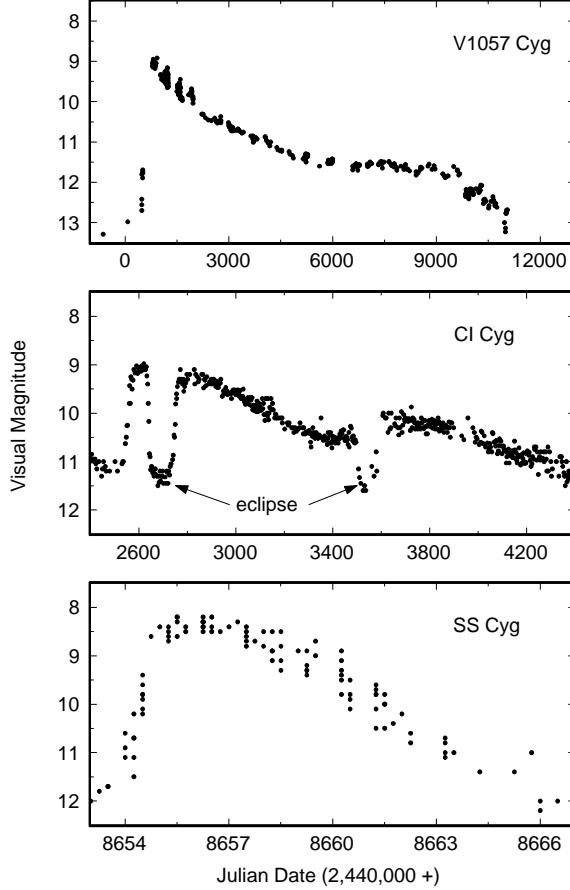

Figure 1 - Light curves for SS Cyg, a cataclysmic binary; CI Cyg, a symbiotic binary; and V1057 Cyg, an FU Ori variable star. Despite a different size scale in each system, the light curves have common features that indicate a similarity in their underlying physics.

As an example of these common phenomena, Figure 1 shows light curves for SS Cyg – a cataclysmic binary with an orbital period of $P_{orb} = 6.6$ hr ([30]); CI Cyg – a symbiotic binary with $P_{orb} = 855$ days ([81], [16]); and V1057 Cyg – an FU Ori variable that is apparently a single star ([84]). The 3–5 mag eruptions of these systems occur when the accretion rate through the disk increases. Aside from the deep eclipses in CI Cyg, the three light curves have common features, with a rapid rise, a brief interval at maximum, and a long decay. All three systems resemble A- or F-type stars

at maximum light. This spectrum cools as the brightness fades. Substantial mass loss is associated with each system; the mass loss probably increases with the rise in brightness and decreases as the brightness declines. These similarities suggest that the same physical processes govern the evolution of disks ranging in size from 0.1 $R_\odot$ to several tens of AU.

TABLE 1. Types of disk systems

System	Distance (pc)	Angular size (arcsec)	N_{res}
BH + MS	1000	$\lesssim 10^{-5}$	100
NS + MS	1000	$\lesssim 10^{-5}$	100
WD + MS	100	$\lesssim 10^{-3}$	100+
MS + SG	100	$\lesssim 10^{-3}$	10+
MS + RG	1000	$\lesssim 10^{-3}$	10–100
β Pic	10+	1–10	10–100
Young star	100+	1–2	10–20
AGN	10^8	$\lesssim 10^{-3}$	1–10

The common features of accreting systems provide good tools to test physical models of disks. Table 1 summarizes the main types of disk-accreting systems known today and provides simple comparisons of their angular sizes and the number of resolution elements across the face of the disk, N_{res}, that can be derived from modern observations. The first set of systems includes (i) compact binaries containing a disk surrounding a black hole (BH), a neutron star (NS), or a white dwarf star (WD), and (ii) wider binaries with a disk surrounding a main sequence star. A low mass main sequence star usually feeds the disk in compact binaries; a more evolved subgiant or red giant star feeds the disk in the wider binaries. In both types of binaries, the angular size of the disk is small compared to the resolution possible with current ground-based or space-based observatories. However, eclipses of the disk by the secondary star can be used to divide the disk into many resolution elements and to map out the physical structure of the disk with a few simplifying assumptions ([70], [71]). The dusty disks in the second group of systems are large enough to image directly at optical and radio wavelengths, although few systems have been mapped in much detail ([164], [77]). The final group of active galactic nuclei have only recently been mapped with VLBI techniques; N_{res} will probably increase as these techniques become more sophisticated ([68]).

2. Steady Disks

Accretion disks work to transport mass radially inwards and angular momentum radially outwards. To understand how a disk manages this feat, consider a thin ring with two adjacent annuli at distances r_1 and r_2 from a central star (Figure 2). Material in these annuli orbits the central star with velocities, v_1 and v_2. The velocity difference between the two annuli, $v_1 - v_2 > 0$, produces a frictional force that attempts to equalize the two orbital velocities. The energy lost to friction heats the annuli; some disk material then moves inwards to conserve total energy. This inward mass motion increases the angular momentum of the ring; some disk material moves outwards to conserve angular momentum. Energy and angular momentum conservation thus lead to an expansion of the ring in response to frictional heating. The ring eventually expands into a disk, which generates heat (and radiation) at a level set by the accretion rate.

Figure 2 - Schematic view of two adjacent annuli in a disk surrounding a compact star. Annulus '1' lies inside annulus '2' and orbits the star (filled circle) at a higher velocity, $v_1 > v_2$.

2.1. ACCRETION LUMINOSITIES AND TEMPERATURES

Figure 3 shows the standard disk geometry. In a *steady* disk, material drifts radially inward at a constant rate, $\dot{M}$. For an infinite disk, the total luminosity generated by accretion is $L_{acc} = GM_\star \dot{M}/R_\star$, which is

$$L_{acc} = 314 \text{ L}_\odot \left(\frac{M_\star}{1 \text{ M}_\odot}\right) \left(\frac{\dot{M}}{10^{-5} \text{ M}_\odot \text{ yr}^{-1}}\right) \left(\frac{1 \text{ R}_\odot}{R_\star}\right) \qquad (1)$$
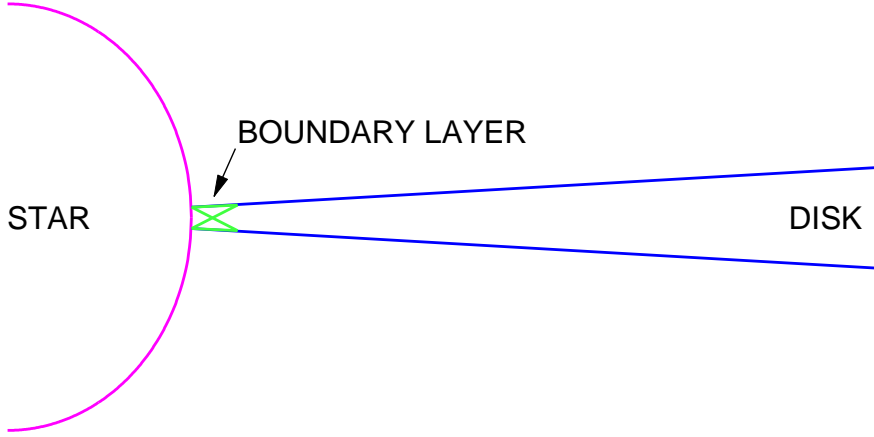
Figure 3 - Schematic view of a disk that extends to the stellar photosphere. Disk material drifts radially inward until it reaches the boundary layer, where the rotational velocity slows to match the stellar rotational velocity.

in familiar units. As material drifts inwards, half of this accretion energy is radiated by the disk,

$$L_{disk} = \frac{1}{2}L_{acc} \ . \tag{2}$$

The other half of the accretion energy becomes kinetic energy of orbital motion around the central star. In most cases, disk material drifts inwards until it reaches the stellar photosphere (Figure 3). At this point, disk material with an angular velocity of $\Omega = (GM_\star/R_\star^3)^{1/2}$ must slow down to match the stellar angular velocity, $\Omega_\star$. This transition occurs in the "boundary layer," a narrow ring with a radial size,

$$R_{bl,d} \sim h_{bl}^2/R_\star \ll R_\star, \tag{3}$$

where h_{bl} is the local scale height ($h_{bl}/R_\star \ll 1$; [138], [140], [141], [132], [96], [143], [95]). The energy lost in the boundary layer is the difference between the rotational energy per unit mass in the disk and the rotational energy per unit mass in the central star:

$$L_{BL} = \frac{1}{2}L_{acc} \left(\frac{\omega_{disk}^2 - \omega_\star^2}{\omega_{disk}^2}\right) \ . \tag{4}$$

In some accreting systems, the magnetic field of the central star is strong enough to truncate the disk at a radius, $R_m > R_\star$. A rough estimate of the truncation radius is the Alfvén radius,
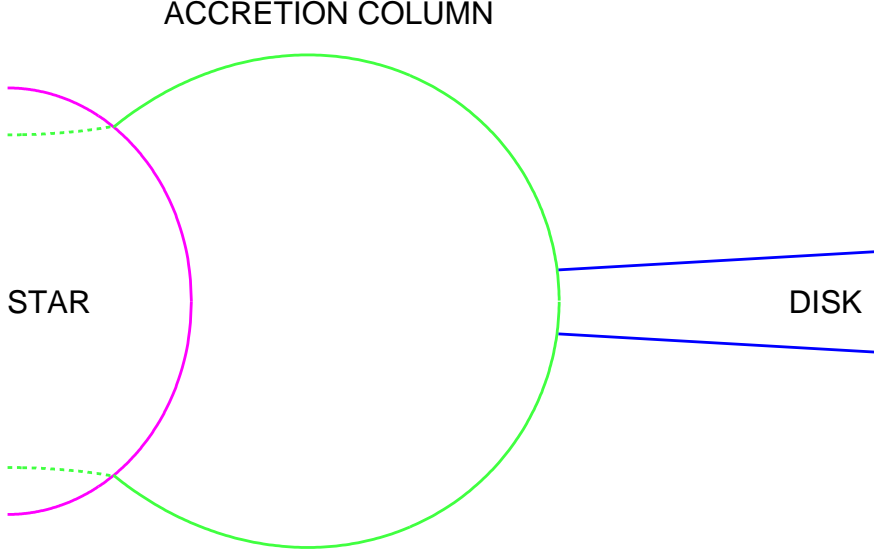
ACCRETION COLUMN

STAR

DISK

Figure 4 - Schematic view of a disk truncated by a strong dipolar magnetic field. The inner radius of the disk lies close to the corotation radius, where the disk and the stellar photosphere have the same angular velocity. Material falls from the inner disk onto the star along the magnetic field lines and produces two circular rings surrounding the magnetic axis.

$$R_m \approx R_A \approx \left(\frac{\mu_\star^4}{2GM_\star \dot{M}^2} \right)^{1/7} \qquad (5)$$

where $\mu_\star$ is the magnetic dipole moment of the central star. More rigorous estimates of R_m depend on the magnetic field geometry ([113], [46], [114], [29], [101], [191], [4], [107], [182]). The disk then has a total luminosity

$$L_{disk} = \frac{1}{2} L_{acc} \left(\frac{R_\star}{R_m} \right) \qquad (6)$$

In this geometry, disk material falls onto the star along magnetic field lines (Figure 4). The infalling gas shocks and produces two rings at stellar latitudes, $\pm b$, if the magnetic and rotational axes are parallel ([46], [101]). These rings are compressed into tilted ellipses if the magnetic axis is inclined with respect to the rotational axis, as expected in most systems ([88], [122]). In both cases, the luminosity of one ring is

$$L_{ring} = \frac{1}{2} L_{acc} \left(1 - \frac{1}{2} \frac{R_\star}{R_{mag}} \right) \qquad (7)$$

To derive the temperature structure of the disk and the boundary layer or magnetic accretion ring, we again use conservation of energy. The disk

temperature assumes an approximate balance between the energy lost from blackbody radiation and the torque due to frictional heating from mass motion through a distance ΔR in a gravitational potential:

$$GM_\star \dot{M} \left(\frac{1}{R} - \frac{1}{R + \Delta R} \right) \approx 2 \cdot 2\pi R \Delta R \ \sigma T_d^4 \qquad (8)$$

For $\Delta R \ll R$, this expression is

$$GM_\star \dot{M} \frac{\Delta R}{R^2} \approx 4\pi R \Delta R \sigma T_d^4 \qquad (9)$$

which results in

$$T_d \approx \left(\frac{GM_\star \dot{M}}{4\pi \sigma R^3} \right)^{1/4} \propto R^{-3/4} \qquad (10)$$

The exact temperature of a steady disk depends on how the torque transports energy through the disk. Standard models assume that frictional heating vanishes at the stellar photosphere, which leads to an extra term in the energy equation (8) above ([120], [161]). The temperature is then ([13]):

$$T_d(R) = T_{acc} \left(\frac{R}{R_\star} \right)^{-3/4} \left(1 - \sqrt{R_\star/r} \right)^{1/4} \qquad (11)$$

where

$$T_{acc} = 13000 \ \text{K} \left(\frac{M_\star \dot{M}}{10^{-5} \ \text{M}_\odot^2 \ \text{yr}^{-1}} \right)^{1/4} \left(\frac{1 \ \text{R}_\odot}{R_\star} \right)^{3/4} . \qquad (12)$$

This expression for the temperature vanishes at the stellar surface, because the frictional heating vanishes. The temperature reaches a maximum at $R/R_\star = 49/36$ ([13]):

$$T_{max} = 6500 \ \text{K} \left(\frac{M_\star \dot{M}}{10^{-5} \ \text{M}_\odot^2 \ \text{yr}^{-1}} \right)^{1/4} \left(\frac{1 \ \text{R}_\odot}{R_\star} \right)^{3/4} \qquad (13)$$

Different boundary conditions at the stellar surface yield slightly different, non-analytic, temperature laws ([134], [135]). These results are usually close to the standard temperature law, equation (11).

The temperature of the boundary layer depends on the mass accretion rate. At high $\dot{M}$, the region is optically thick ([120], [174]). Energy generated in the thin "dynamical boundary layer" (equation 3) should diffuse over a broader ring with a size comparable to the thermal scale height, h_{bl} ([132]). The scale height is smaller than the stellar radius in most cases. This "thermal boundary layer" is then much larger than the dynamical

boundary layer and has a temperature 4–5 times larger than the maximum disk temperature ([91]). For low $\dot{M}$, the boundary layer is optically thin and cannot radiate energy efficiently ([138], [140]). The thermal scale height is then comparable to the stellar radius, and the boundary layer resembles a hot stellar corona ([138], [140]). The details of boundary layer structure are sensitive to properties of the stellar photosphere and the viscosity mechanism, but these general considerations hold for many physical settings ([18], [17], [136], [72], [73], [47], [48], [137], [76], [97], [98]).

   The temperature of magnetic accretion rings also depends on geometry. If the magnetic axis is aligned with the rotational axis, the rings have equal luminosities and temperatures. The temperature is also constant with azimuth along each ring ([122]). The two rings have unequal luminosities when the magnetic axis is tilted with respect to the rotational axis, as needed to produce the observed light variations in magnetic cataclysmic variables and T Tauri stars ([36], [88]). The luminosity also varies with azimuth along each ring ([122]). In the aligned case, the infalling matter shocks above the stellar surface and forms identical optically thick accretion columns that radiate in the Balmer and Paschen continua ([104], [26]). The surface area of this emission is comparable to the surface area of the boundary layer, so the temperature is still 3–5 times larger than the maximum disk temperature ([26]). The accretion columns are probably quite different in non-aligned cases, but their structure has not been addressed.

TABLE 2. Accretion and nuclear energies

Object	ϵ_g (erg g^{-1})	ϵ_{nuc} (erg g^{-1})
T Tauri star	5×10^{14}	5×10^{13}
main sequence star	2×10^{15}	4×10^{18}
white dwarf star	1×10^{17}	4×10^{18}
neutron star	1×10^{20}	6×10^{18}

   To judge the effectiveness of accretion as an energy source, Table 2 compares the gravitational potential energy, $\epsilon_g = GM_\star/R_\star$, of various 1 $M_\odot$ stars with the nuclear energy generation rate of the dominant fusion source, ϵ_{nuc}. If a star can accrete *and burn* material from a disk, then the ratio of the accretion luminosity to the nuclear luminosity is simply the ratio of these two quantities, $r \equiv L_{acc}/L_{nuc} = \epsilon_g/\epsilon_{nuc}$. This expression ignores the difference in accretion and nuclear time scales, but it provides a simple guide to the importance of accretion as a long-term energy source. Table 2 shows that accretion is rarely the major energy source for main sequence stars and white dwarfs; nuclear energy will always overwhelm accretion by factors of 40–2000 on long time scales. Accretion is an excellent energy source for pre-main sequence stars and neutron stars. It is roughly 10 times more effective than deuterium burning in pre-main sequence stars

and nearly 20 times more productive than complete hydrogen burning in neutron stars.

2.2. TURBULENT VISCOSITY AND DISK TIMESCALES

The source of the frictional heating in accretion disks remains controversial. Ordinary molecular viscosity is too small to generate mass motion on a reasonable time scale, $\sim$ days for disks in interacting binary systems and $\sim$ years to decades for disks in pre-main sequence stars. The large shear between adjacent disk annuli suggests that disks might be unstable to turbulent motions, which has led to many turbulent viscosity mechanisms. Convective eddies, gravitational instabilities, internal shocks, magnetic stresses, sound waves, spiral density waves, and tidal forces have all been popular turbulence mechanisms in the past three decades (see, for example, [120], [161], [25], [112], [176], [7], [60], [172], [168], [24], [177], [157], [144], [5]).

Recent work has shown that magnetic stresses in a differentially rotating disk inevitably lead to turbulence ([9], [8], [110]). The growth time and effectiveness of these magnetohydrodynamic mechanisms make them the current leading candidate for viscosity in most applications. How this turbulence leads to significant mass motion in a real accretion disk remains an unsolved problem.

Shakura & Sunyaev side-stepped the basic uncertainties of viscosity mechanisms when they developed the popular "α-disk" model ([161]; see also [179]). In this approach, the frictional heating in the disk is due to a turbulent viscosity, $\nu = \alpha c_s h$, where c_s is the sound speed, h is the local scale height of the gas, and α is a dimensionless constant. This concept is similar to the mixing length theory of convection, with α serving the role of the mixing length. In most applications, $\alpha \lesssim 1$–10; α needs to exceed $\sim 10^{-4}$ to allow material to move inwards on a reasonable time scale.

This viscosity definition orders the important time scales for the disk ([120]). The shortest disk time scale is the dynamical (orbital) time scale, which increases radially outward:

$$\tau_D \approx 0.1 \text{ day } \left(\frac{R}{1 \text{ R}_\odot}\right)^{3/2} \left(\frac{1 \text{ M}_\odot}{M_\star}\right)^{1/2} \tag{14}$$

The thermal time scale measures the rate that energy diffuses through the disk,

$$\tau_T \approx 1 \text{ day } \left(\frac{R}{1 \text{ R}_\odot}\right)^{11/8} . \tag{15}$$

The thermal time scale is intermediate between the dynamical time scale and the viscous time scale, which measures the rate matter diffuses through the disk,
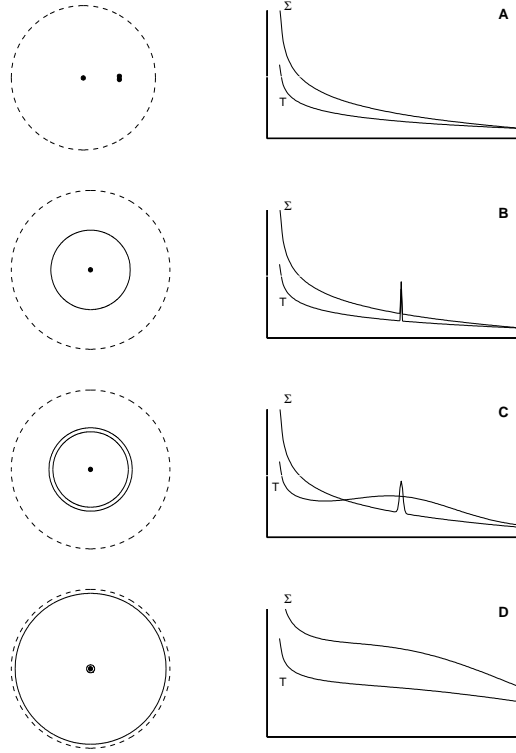
Figure 5 - Schematic evolution of a point-like mass enhancement, a blob, in a viscous accretion disk. A central star lies at the center of the disk with an outer edge indicated by the dashed circle. The disk initially has a smooth radial decrease in the effective temperature, T, and the surface density, Σ (panel A). Differential rotation between adjacent annuli smooths the blob into a ring on the orbital time scale, τ_D, which produces δ-function increases in T and Σ (panel B). The thermal energy in the blob moves inwards and outwards on the thermal time scale, τ_T, which produces a gaussian-like perturbation in the temperature (panel C). The mass motion on this time scale is small; Σ changes little on the thermal time scale. The mass perturbation spreads out through the disk on the viscous time scale, τ_V, as indicated in panel D.

$$\tau_V \approx \frac{40 \text{ day}}{\alpha} \left(\frac{R}{1 \text{ R}_\odot}\right)^{5/4} \tag{16}$$

Figure 5 illustrates the evolution of the disk on these time scales. The top panel shows a blob of material superimposed on the smooth density and temperature structure of a steady disk. In this example, the blob has a mass, δM, larger than the mass of an annulus, and a thermal energy content, δE, larger than the local thermal energy of an annulus. Disk rotation broadens the blob into a narrow ring in one or two rotation periods, which produces a narrow spike in the radial distributions of surface density and temperature. The thermal energy of this ring moves inwards and outwards on the thermal

time scale. The temperature distribution broadens considerably, but the surface density hardly changes. The mass in the ring finally moves inwards and outwards on the viscous time scale. This evolution produces an extra increase in the temperature due to viscous dissipation.

Table 3 compares numerical values for the three disk time scales. These results assume $M_\star = 1\,\mathrm{M}_\odot$ and $\alpha = 10^{-1}$. For most interacting binaries, the disk radius is ~ 0.1–$10\,\mathrm{R}_\odot$; the time scales range from a fraction of a day for τ_D up to several tens of days for τ_V. The time scales increase dramatically for the larger disks in pre-main sequence stars and active galactic nuclei. The viscous time scale at the edge of a typical solar system is comparable to the disk lifetime.

TABLE 3. Disk time scales

Disk radius	h/r	T (K)	τ_D	τ_T	τ_V
0.1 $\mathrm{R}_\odot$	0.02	2×10^4	0.004 d	0.04 d	20 d
1.0	0.02	5×10^3	0.120 d	1.00 d	400 d
1 AU	0.04	250	1 yr	4 yr	1×10^4 yr
10	0.06	60	32 yr	105 yr	1×10^5 yr
100	0.08	25	1000 yr	2500 yr	2×10^6 yr

2.3. DISK ENERGY DISTRIBUTIONS

Figure 6 shows the broadband spectral energy distribution of a steady accretion disk with a boundary layer. The model assumes that the disk is optically thick and that each annulus radiates as a blackbody ([120], [13], [174], [158]). There are two main features in this spectrum: (i) radiation from the boundary layer at short wavelengths, and (ii) disk radiation at longer wavelengths. If the disk has a large ratio of outer radius to inner radius, $R_{out}/R_{in} \gg 1$, the disk spectrum follows

$$\lambda F_\lambda \propto \lambda^{-4/3} \qquad\qquad \lambda_{in} < \lambda < \lambda_{out} \qquad (17)$$

where $\lambda_{in} T_d(R_{in}) \approx \lambda_{out} T_d(R_{out}) \approx 0.36$ ([120]). The disk spectrum follows the Wien tail of a hot blackbody, $T_d(R_{in})$, at short wavelengths and the Rayleigh-Jeans tail of a cool blackbody, $T_d(R_{out})$, at long wavelengths.

Although Figure 6 assumes a blackbody disk, the general features of the model change little if the disk radiates as some type of stellar atmosphere. The most important modifications for pre-main sequence stars involve irradiation from the central star and the infalling envelope, as described by Beckwith in this volume.
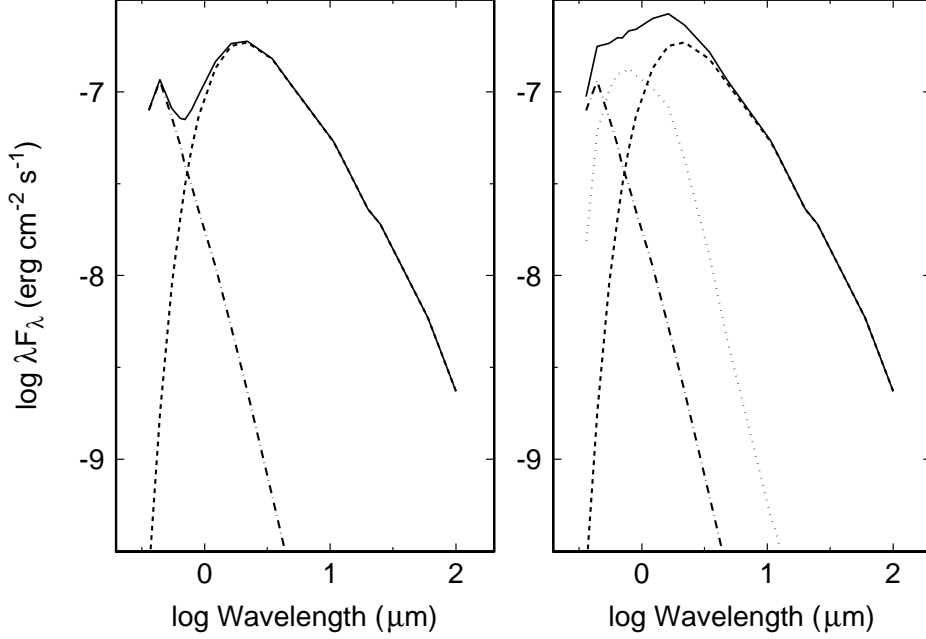
Figure 6 - Energy distributions for accretion disks. The left panel shows the energy distribution of a disk (dashed line), a boundary layer (dot-dashed line), and the total energy output (solid line) for $\dot{M} = 2 \times 10^{-7}$ $M_\odot$ yr^{-1} onto a solar-type star. The right panel adds the energy distribution (dotted line) for a star with $L_\star \approx L_d$.

Lynden-Bell & Pringle first applied these concepts to disks in interacting binaries and pre-main sequence stars. They added radiation from the central star to the spectrum, as indicated in the right panel of Figure 6. This model suggests that identifying disk radiation can be difficult when the stellar luminosity exceeds the accretion luminosity. Table 4 compares temperatures and luminosities of pre-main sequence stars and steady disks for two accretions rates, $\dot{M} = 10^{-6}$ and 10^{-4} $M_\odot$ yr^{-1}. At low masses, the contrast between the disk and star is considerable unless the accretion rate is $\lesssim 10^{-8}$ $M_\odot$ yr^{-1}. This contrast decreases for more massive stars. At 10 $M_\odot$, the star is hotter and as luminous as the disk, because massive young stars burn hydrogen before reaching the main sequence. Table 3 shows that accretion cannot be a dominant energy source for main sequence stars; the difficulty of seeing an accretion disk against the background of a young O or B star therefore is not surprising.

3. Unstable Accretion Disks

Despite the elegant simplicity of the steady-state model, all disks vary their energy output. These fluctuations range from small, 10%–20%, amplitude flickering on the local dynamical time scale ([23]) to large-scale eruptions,

TABLE 4. Accretion and stellar luminosities in pre-main sequence stars

$M_\star(M_\odot)$	$T_\star$(K)	$L_\star$($L_\odot$)	10^{-6} $M_\odot$ yr^{-1}		10^{-4} $M_\odot$ yr^{-1}	
			T_{max} (K)	L_{acc} ($L_\odot$)	T_{max} (K)	L_{acc} ($L_\odot$)
0.1	3100	0.1	1850	3	5850	275
0.4	3600	0.5	1825	7	5800	675
1.0	4250	7.0	1800	12	5700	1200
3.0	8650	80	1700	25	5350	2350
6.0	17000	1000	2100	50	6650	5000
10.0	21000	5000	1850	60	5850	6000
20.0	29000	45000	1600	75	5000	7450

$\sim$ 3–5 mag or more, that can last for several times the local viscous time scale (Figure 1). In well-studied dwarf novae, the outbursts occur in cyclical patterns with quasi-periods of 10 or more days ([30], [130]).

Osaki and Pringle *et al.* first noted the possibility for thermal instabilities in accretion disks ([139], [131]). In the standard picture, the structure of a steady disk is derived from balancing heat generated by viscosity with radiative cooling. However, the viscous energy generation and radiative losses are set by local disk parameters; the input $\dot{M}$ is an external parameter. Cooling can balance heating only if the local physical quantities can adjust to the input $\dot{M}$. If the local physical variables cannot adjust, cooling cannot balance heating and a thermal instability is likely.

Figure 7 displays a simple illustration of a thermal instability in a single disk annulus. The solid curves indicate loci of stable disks, where cooling precisely balances heating. To the right of these lines, heating exceeds cooling because viscous energy generation – set by the local surface density Σ through $\dot{M} = \nu\Sigma$ – exceeds the radiative losses set by the effective temperature, T_d. Cooling exceeds heating to the left of the stability lines.

To illustrate the evolution of the instability, assume the annulus has (Σ, T_d) at A′ and an input accretion rate, $\dot{M}_1$. This input accretion rate exceeds the stable accretion rate at A′, $\dot{M}_s = \dot{M}_{A'}$. The annulus evolves up the solid line on the viscous time scale to find a solution where $\dot{M}_s = \dot{M}_1$. Before reaching this point, the annulus arrives at $\dot{M}_B$, the last stable solution for this opacity source. At B, the annulus needs a larger surface density to accommodate the larger $\dot{M}$, and a larger T_d to radiate away the extra heat generated by the larger $\dot{M}$. To do so, the annulus evolves to C; it makes this transition at constant Σ because the thermal time scale is shorter than the viscous time scale. Once at C, the annulus radiates more energy than generated by viscous dissipation ($\dot{M}_s = \dot{M}_C > \dot{M}_1$) and evolves down the solid line towards a solution where $\dot{M}_s = \dot{M}_1$. The annulus moves towards

lower Σ on the viscous time scale until it reaches point D, the last stable solution on this branch of the equilibrium curve. At D, the annulus drops to A to try to find the smaller T_d needed to accommodate a smaller $\dot{M}$. Once at A, the annulus retraces the steps around this 'limit-cycle' curve as long as $\dot{M} = \dot{M}_1$.
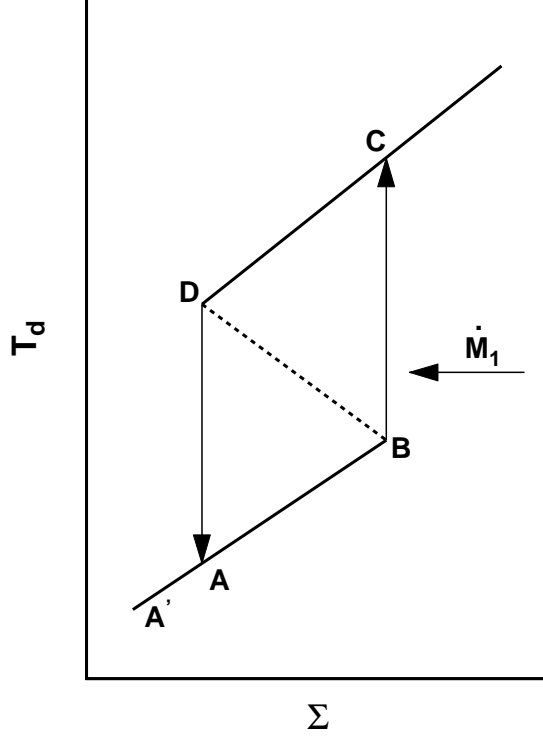

Figure 7 - Outline of a disk instability in a single annulus. The disk evolves along the solid lines ABCD for an input $\dot{M}$ (horizontal arrow). Heavy solid lines correspond to stable equilibrium solutions; a dashed line indicates the locus of unstable equilibria.

The evolution of an instability in a complete accretion disk follows the simple illustration. In a real disk, most annuli are close to B when a single annulus makes the transition from B to C. The increased temperature of a single annulus transfers heat to neighboring annuli on the thermal time scale; these annuli then jump to the 'high state' and propagate the eruption to their neighbors. Figure 8 shows this evolution for five snapshots in the evolution of a dwarf nova accretion disk. Time increases upwards in the Figure. The bottom panel shows the temperature distribution of the disk at the onset of the eruption. The inner edge of the disk jumps to the high state first; annuli at larger radii progressively follow until all of the disk resides in the high state in the top panel. The disk maintains this state for several days, and then retraces its path back to the low state.
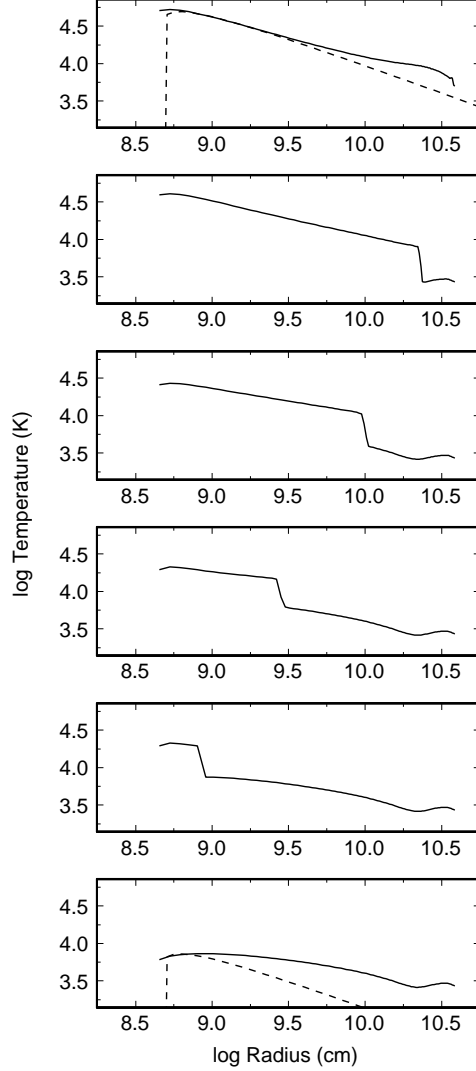
15

Figure 8 - Evolution of a disk instability in a dwarf nova disk. The bottom panel compares the radial temperature distribution of a time-dependent disk (solid line) with the temperature distribution of a steady disk (dashed line). The eruption begins in the next panel with a sharp increase in the temperature at the inner edge of the disk. This increase creates a 'wave' of increased temperature that propagates radially outwards in the disk as time moves forward (up in the figure). In the top panel, the entire disk has reached the hot state; the actual temperature distribution (solid line) is then close to the steady-state temperature distribution (dashed line)

One feature of the disk instability picture is that the disk is never in a steady-state. The dashed lines in Figure 8 plot steady-state temperature distributions normalized to the temperature at the inner edge of the disk.

The actual temperature gradient is much flatter than the steady-state gradient in the low state (bottom panel). The $\dot{M}$ through the disk increases radially outwards and is below the input $\dot{M}$ at each point in the disk. The disk approaches but never reaches the steady-state gradient in the high state (top panel).

Actual disk temperature distributions have been derived from eclipse light curves similar to those shown in Figure 1 for CI Cyg. K. Horne & collaborators ([70], [71], [125], [10]) have used maximum entropy techniques to recover $T_d(R)$ from multi-wavelength light curves and spectroscopic data assuming (i) the disk is azimuthally symmetric and (ii) the brightness temperature is close to the local blackbody temperature. Their results indicate that quiescent disks are rarely close to steady-state, with temperature distributions usually much flatter than $T_d(R) \propto R^{-3/4}$. Systems in eruption – dwarf novae and symbiotic stars at maximum light – more closely resemble, but never achieve, the steady-state temperature distribution with $q = 3/4$. These results generally agree with the model predictions in Figure 8.

4. Disk Eruptions in Pre-Main Sequence Stars

Most pre-main sequence stars vary in brightness. Irregular brightness variations of $\lesssim 1$ mag are a defining feature of T Tauri stars and many Herbig AeBe stars ([78], [61]). Recent studies show that many of these variations are due to dark spots rotating with the stellar photosphere ([66], [21], [22], [67]) or bright spots produced at the base of a magnetic accretion column ([21], [88]). Small eruptions of 1–3 mag lasting several years occur in the EXors, a poorly-studied class which includes EX Lup and DR Tau ([64]). More spectacular 3–6 mag eruptions occur in the FU Orionis variables, also known as FUors ([63], [59]).

G. Herbig first associated the eruptions of FUors with pre-main sequence stars ([62], [63]; see also [3], [94]). FU Ori, which lies at the apex of a fan-shaped nebula within the dark cloud B35, brightened by a factor of over one hundred in 100–200 days (Figure 9; [180], [181], [62], [63], [74], [162], [75]). Thirty years later, Welin discovered the 5 mag brightening of V1057 Cyg within an eccentric ring of reflection nebulosity (Figure 9; [185], [63], [84], [99]). Herbig later noted the similarity between the optical spectra of these two stars with spectra of V1515 Cyg, a faint variable star embedded in arc-shaped nebulosity ([61]). He collected archival photographic photometry and identified a slow rise from $m_{pg} \approx 15.5$ in the late 1940s to $m_{pg} \approx 13.5$ in the late 1970s ([63]). This brightness increase continued until 1980, when the star experienced a dramatic decline and slow recovery ([100], [90]).

Herbig's demonstration that FU Ori – and by analogy other FUors – is a pre-main sequence star is straightforward. FUors are clearly associated with dark clouds, having radial velocities indistinguishable from the cloud velocity. The optical spectrum, including the high lithium abundance, has similarities with spectra of T Tauri stars. The event statistics are plau-

sible for pre-main sequence stars. Finally, the rise in brightness is a real luminosity increase that is *not* a nova outburst, the main alternative.
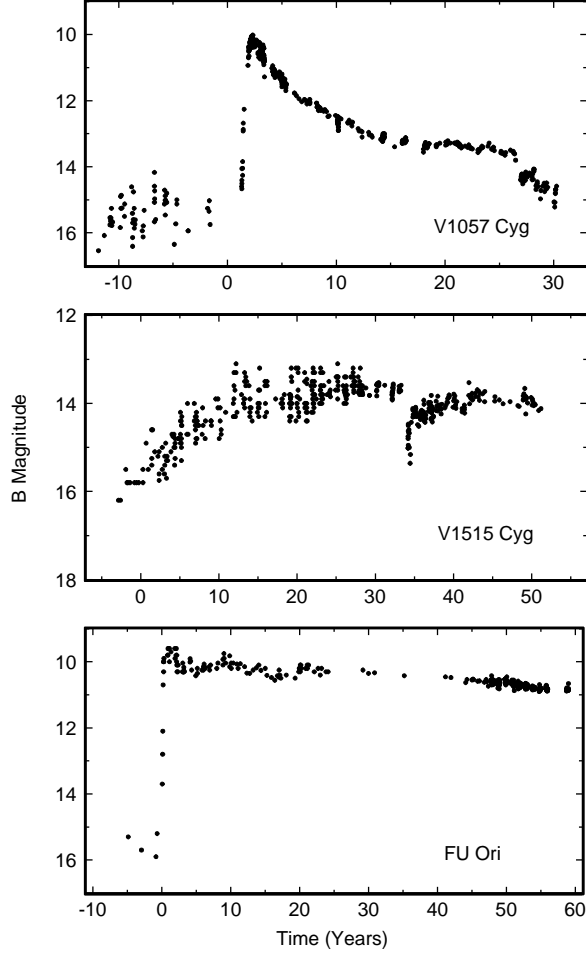

Figure 9 - Blue light curves for three FU Ori variables.

Many new FUors have been discovered since V1515 Cyg. The catalogued number now stands at 11 ([59], Table 5). Most have been observed to rise 3–5 mag in optical or near-IR brightness in less than one year, as indicated by the 'Y' in the outburst (OB) column of Table 5. V1515 Cyg is the only known example to require a decade to rise to visual maximum, but the historical light curves for some systems are poorly documented. A few objects have been called FUors based on common spectroscopic properties, which are described more completely below. Most recent FUors are more intimately associated with the densest dark clouds than the first members of the class, which suggests that many eruptions might have been missed.

There are also 3 candidate FUors listed as a second group of objects in Table 5. These objects have some properties in common with FUors, but more data are needed to see if they have the other characteristics as well ([169], [159]). A few other objects have one or two properties of known FUors, such as an outburst or unusual light curve (e.g., [41], [69], [2], ([163], [192]). These are more probably EXors or Ae/Be stars than FUors.

4.1. BASIC PROPERTIES OF FU ORIONIS OBJECTS

FUors share a distinctive set of morphological, photometric, and spectroscopic characteristics (Table 5). Three are known binary stars, L1551 IRS5, Z CMa, and RNO 1B/1C ([102], [86], [11], [171], [156]). Most have delicate fan-shaped or comma-shaped reflection nebulae (RN) on optical and near-IR images ([50], [148], [127], [118]). Optical jets and HH objects are common ([148], [38], [59]). Most appear associated with large-scale molecular outflows ([189], [43], [42], [121], [190], [44], [117], and references therein). These features – together with the broad, blue-shifted Na I and H I absorption features described below – demonstrate that FUors drive powerful winds that interact with the surrounding medium ([12], [37], [188]).

TABLE 5. Selected properties of FU Orionis objects

Object	OB	Opt ST	IR ST	RN	HH/Jet	Wind	Outflow	Radio
L1551 IRS 5	?	K	M	Y	Y	?	Y	Y
FU Ori	Y	F–G	M	Y	N	Y	N	N
Z CMa	?	F–G	M	Y	Y	Y	Y	Y
BBW 76	@	G	M	Y	?	Y	N	?
V346 Nor	Y	?	C	Y	Y	?	Y	?
Par 21	?	F	M	Y	Y	Y	?	?
V1515 Cyg	Y	G	M	Y	N	Y	Y	N
V1057 Cyg	Y	G	M	Y	N	Y	Y	Y
V1735 Cyg	Y	?	M	Y	N	?	Y	Y
RNO 1B/1C	Y	G	M	Y	N	?	Y	?
IC 430	?	G	?	Y	Y	Y	N	Y
PP 13S	Y	?	M	?	?	?	Y	?
Re 50	?	G	?	Y	Y	Y	Y	Y

FUors also have very unusual spectroscopic characteristics. The optically visible sources have F–G, and sometimes K-type, giant or supergiant spectra ([63]; Table 5, see also [58], [149], [153])). The optical reflection nebulae of several embedded FUors also show G-type absorption features ([167], [166]). All FUors but Z CMa and V346 Nor have very deep CO absorption bands on near-IR spectra at 1.6 μm and 2.3 μm ([126], [40], [31],

[160], [82], [19]). These features resemble the CO absorption bands observed in red giants and are much stronger than those observed in any other pre-main sequence star ([56], [57], [51]). CO absorption in Z CMa is weakened by dust emission from an embedded companion; V346 Nor has weak CO emission instead of CO absorption ([102], [170]; [153]). Many FUors also display strong water absorption features, which strengthens the evidence for a ~ 2000 K photosphere ([27], [160], [28]).

All FUors show large *excesses* of radiation over normal G supergiants at both ultraviolet and infrared wavelengths. The near-IR excess is clearly photospheric in origin, because the CO and H_2O absorption features are so intense. The UV excesses in Z CMa and FU Ori appear associated with an A- or F-type photosphere that is hotter than the G-type photosphere observed at longer wavelengths ([89]). In addition to significant far-IR and submm emission ([183], [184], [84]), many FUors are strong radio continuum sources at cm wavelengths ([35], [154], [155], [116], [156]). This emission is not photospheric in some FUors and may be produced in the outflow or the jet.

Herbig first noted broad absorption lines on optical spectra of several FUors ([63]). Hartmann & Kenyon later confirmed large rotational velocities of $v \sin i \approx 15$–60 km s^{-1} for V1057 Cyg, V1515 Cyg, and FU Ori ([55]). This property is now characteristic of the class; all FUors have broad optical or infrared absorption lines or both ([58], [165], [166], [82]). The rotational velocity further depends on wavelength. The near-IR CO lines in FU Ori and V1057 Cyg have significantly smaller rotational velocities than the optical lines ([56], [57]). The optical rotational velocity smoothly increases with decreasing wavelength in Z CMa and V1057 Cyg ([186], [187]). In FU Ori itself, a powerful wind masks weak absorption lines and makes it difficult to detect any variation of rotational velocity with wavelength should one exist.

Many FUors display *doubled* absorption lines on optical and near-IR spectra ([55], [56], [57], [58], [165], [166]). The two absorption components in V1057 Cyg are separated by 30–40 km s^{-1}; these features have much larger separations in Z CMa and FU Ori. The long-term stability of the doubled absorption lines indicates that the lines are not produced by two stellar components in a binary system ([87]).

Most FUors also show strong evidence for mass loss, in addition to the HH objects and CO outflows described above. Practically every FUor displays deep, blueshifted absorption components on Hα and Na I D ([12], [37], [39], [187], [54]); weak blueshifted CO absorption might be present in FU Ori ([57]). The optical line profiles can also change on month to year time scales ([12], [37], [187]). The near-IR line profiles may also change ([19]). Both V1057 Cyg and V1515 Cyg have very pronounced line profile changes and dips in their optical light curves. These fluctuations suggest dust formation in a variable wind, but the data are not very extensive ([90]).

Finally, FUor eruptions must be repetitive ([63], [55]). The event statistics of known FUors suggest that a young star must undergo 10–20 FUor

eruptions before reaching the main sequence. This estimate may be a lower limit, because some outbursts have certainly been missed. Reipurth's proposal that FUor eruptions produce HH objects suggests a recurrence time scale of ~ 1000 yr, based on the identification of multiple bowshocks (ejection events) with dynamical separations of 500–2000 yr ([145], [146], [53], [152], [6]). The discovery of giant HH flows with dynamical time scales of 10^4–10^5 yr ([151]) allows 10–100 eruptions if eruptions actually power the outflow (see below).

4.2. FU ORIONIS OBJECTS AS ACCRETION DISKS

The observations described above place severe constraints on possible FUor outburst mechanisms. With a luminosity of a few hundred $L_\odot$ (Table 6), a typical FUor emits 10^{45} to 10^{46} erg during the course of a 10–100 yr eruption. Outbursts also recur every 10^3–10^5 yr. This process produces an object resembling a rapidly rotating F-G supergiant in the optical and a more slowly rotating M giant in the infrared. It must be unique to young stars, because we have not observed a FUor event in an older star system.

Accretion is the most plausible energy source for FUor eruptions ([55], [109]). By analogy with dwarf novae, FUor eruptions are the high state of a thermal instability in a disk surrounding a pre-main sequence star. This instability occurs if the accretion rate from the molecular cloud core into the disk lies between the stable accretion rates in the low state and the high state (Figure 7). The system cycles between these two states as long as the surrounding cloud can replenish the disk between outbursts.

TABLE 6. Disk Properties of FU Orionis Objects

Object	L_{bol} (L$_\odot$)	$M_\star \dot{M}(10^{-5}$ M$_\odot^2$ yr$^{-1})$	$R_\star$(R$_\odot$)
L1551 IRS 5	30	0.1	0.4
FU Ori	220	1.7	1.2
Z CMa	400	4.0	1.6
BBW 76	200	1.4	1.1
V346 Nor	160	1.0	1.0
Par 21	200	1.4	1.1
V1515 Cyg	135	0.8	0.9
V1057 Cyg	400	4.0	1.6
V1735 Cyg	200	1.3	1.1
RNO 1B/1C	750	3.5	1.5

Table 6 lists the disk properties needed to power observed FUor luminosities from accretion. To make these estimates, I assume a steady disk

with $L_{disk} = 157 \ \mathrm{L}_\odot (M_\star \dot{M}/R_\star)$ and $T_{max} \approx 6500 \ \mathrm{K} \ (M_\star \dot{M}/R_\star{}^3)^{1/4}$. Combining these and setting $T_{max} = 6500 \ \mathrm{K}$ for an F-G supergiant star yields

$$R_\star \approx \left(\frac{L_{disk}}{157 \ \mathrm{L}_\odot} \right)^{1/2} \qquad (18)$$

and

$$M_\star \dot{M} \approx \left(\frac{L_{disk}}{157 \ \mathrm{L}_\odot} \right)^{3/2} \qquad (19)$$

These expressions produce the results in Table 6 for known FUors, assuming a typical inclination angle, $\cos i = 1/2$. The median inner radius for the FUor sample is $R_\star \approx 1.1$–$1.2 \ \mathrm{R}_\odot$; the median mass accretion rate is $M_\star \dot{M} \sim 1$–$2 \times 10^{-5} \ \mathrm{M}_\odot^2 \ \mathrm{yr}^{-1}$. For a mass-radius relation for pre-main sequence stars with ages of 10^5 yr, $M_\star \approx 0.2$–$0.3 \ \mathrm{M}_\odot$ and $\dot{M} \approx 0.5$–$1 \times 10^{-4} \ \mathrm{M}_\odot \ \mathrm{yr}^{-1}$.

This very simple analysis indicates that a young star must accrete material at $\sim 10^{-4} \ \mathrm{M}_\odot \ \mathrm{yr}^{-1}$ during an eruption to power the observed luminosity. For an adopted outburst duration of 100 yr, this accretion rate results in a total accreted mass of $\sim 0.01 \ \mathrm{M}_\odot$ per eruption. The total mass accreted during a FUor eruption must be replenished during a low state lasting $\sim 10^3$–10^5 yr, which results in an infall rate of $\sim 10^{-5}$–$10^{-7} \ \mathrm{M}_\odot \ \mathrm{yr}^{-1}$. This range is close to the infall rates envisioned – and in some cases observed – for typical cloud cores ([1], [128], [124]).

4.3. OBSERVATIONAL TESTS OF DISK MODELS

Steady accretion disk models successfully explain many observations of FUors ([55], [87], [59]). Theoretical models of disk instabilities produce eruptions that generally resemble FUor events, although comparisons with observations are still in their early stages ([109], [32], [33], [80], [14], [15], [34], [129], [173]). The next few paragraphs summarize these results; Herbig & Petrov present a different interpretation ([65], [133]; see also [106]).

Figure 10 shows light curves for V1057 Cyg, one of the best-studied FUors. These light curves closely resemble those of other accreting systems and provide strong support for an accretion model ([87], [33], [84], [15], [34], [111], [173]). The amplitude of the decline is largest in the UV and decreases monotonically from 0.3 μm to 5 μm. This behavior is characteristic of accreting systems, which evolve towards cooler temperatures as the luminosity declines ([91], [15], [111], [30]). The spectral type variation also agrees with disk model predictions. If we assign stellar effective temperatures to the optical spectrum at maximum (A5 star) and at the current epoch (G5 star), the UBV decline indicates a source with a roughly constant radius. This requirement is easy to achieve with an accretion disk if the radius of the central star remains constant. Most stars cannot evolve at constant radius if their effective temperatures change.
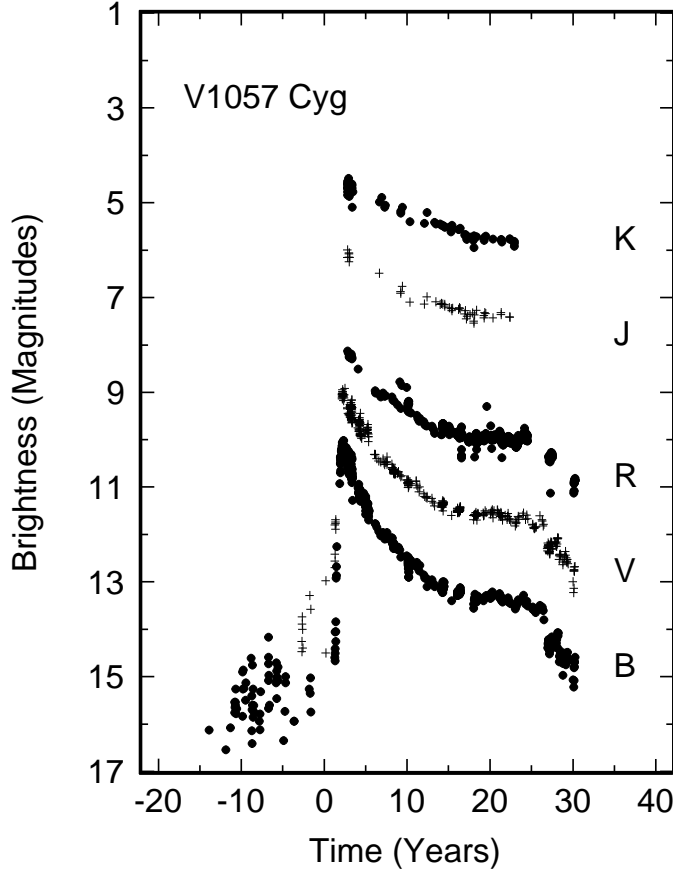
22

Figure 10 - Light curves for V1057 Cyg. The symbols alternate between filled circles (at B, R, and K) and plus signs (V and J). The system varied erratically at B = 14–17 prior to outburst and then rose 5–6 mag in less than one year. The visual observations indicate a similar rise time, although few pre-outburst observations are available. No pre-outburst near-IR data exist; K-band observations began shortly after the outburst was detected. The amplitude of the decline clearly depends on wavelength, with larger amplitudes at shorter wavelengths (see [84], [162], [99]).

The light curves of other FUors also generally agree with disk model predictions. The rise times of 200–400 days in FU Ori and V1057 Cyg are comparable to the thermal time scale, as expected for an eruption that begins at the inner edge of the disk (Table 3; [15]). The several decade rise in V1515 Cyg is too long for such an "inside-out" instability, but could be caused by an outburst that begins in the outer part of the disk . These "outside-in" eruptions can result from perturbations of the disk by a companion star or planet, in addition to the disk instability mechanism described above ([33], [20], [15], [34]). In all systems, the decay times are comparable to the viscous time scale (Table 3).
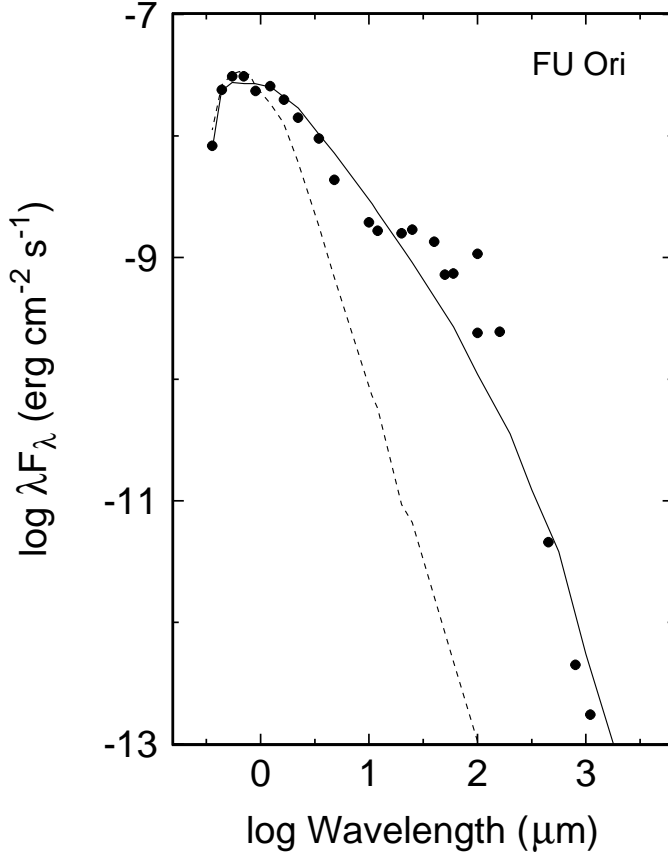
Figure 11 – Spectral energy distribution for FU Ori. The observations (filled circles) indicate a clear excess over a G-type star (dashed line). A disk model that produces a G-type optical spectrum accounts for most of the data (solid line). The modest far-IR excess over the disk spectrum at ~ 100 μm is probably produced by the surrounding nebula responsible for the fan-shaped reflection nebula.

Disk models also successfully explain FUor SEDs ([55], [87], [84]). Figure 11 shows a dereddened SED for FU Ori. The deep UV and near-IR absorption features indicate that the UV and IR excesses over a G-type supergiant spectrum are photospheric ([27]). If disks radiate like stars at the effective temperatures appropriate for the observed absorption features, the SEDs for FU Ori and other FUors require that the surface area of the emitting region increases with increasing wavelength. In particular, the surface area of the near-IR source must be 10–20 times larger than the surface area of the optical source; the 300 K material responsible for the 10 μm excess must have roughly 100 times the emitting area of the optical continuum region. A disk in which the temperature decreases radially outward (§2) naturally explains this observation. Disk models account for the 0.3–10 μm SEDs of V1057 Cyg, V1515 Cyg, and FU Ori quite well (Figure 11; see also

[55], [1], [87], [84], [15], [173]). Several other FUors with modest reddening have similar SEDs ([84]).

Recent interferometric observations have resolved FU Ori at near-IR wavelengths. The angular size at 2.2 μm agrees with predictions of the accretion disk model ([123]).

The disk model *fails* to explain 10–100 μm data of many FUors, although the model fits both FU Ori and BBW 76 from 1–100 μm ([84]). However, the decline of the 10–20 μm light of V1057 Cyg follows the optical light curve very closely ([84]). This behavior suggests that the mid-IR radiation is optical light absorbed and reradiated by a surrounding envelope. An infall rate of 1–5 $\times$ 10^{-6} M$_\odot$ yr^{-1} produces an optically thick envelope that can reprocess optical light from the inner disk and account for the 10–100 μm SED ([84], [15]). This rate is sufficient to replenish the disk in 1000 yr, which allows recurrent FUor eruptions in this system. The observational evidence for infall at comparable rates in two FUors, Z CMa ([108]) and L1551 IRS5 ([128], [124]), lends support to this interpretation.

Finally, an accretion disk also naturally explains the optical and IR line profiles observed in some FUors ([56], [57], [87], [58], [186], [187]). The gradual decrease in the rotational velocity with increasing wavelength occurs because the longer wavelength emission is produced in more slowly-orbiting material at larger disk radii than the more rapidly moving inner disk material responsible for the short wavelength emission. At a given disk temperature, a larger fraction of the disk surface rotates at high line-of-sight velocities and the lines appear doubled ([87], [28], [137]).

4.4. THE IMPORTANCE OF FU ORI ERUPTIONS

Despite their relative rarity, FUors are an important part of pre-main sequence stellar evolution. FUor eruptions add a significant fraction of a stellar mass to the central star. FUor eruptions also eject a large amount of mass into the surrounding cloud. FUor eruptions may be frequent enough to provide nearly all of the mass of a typical low mass star. If this hypothesis is correct, FUor eruptions can power most molecular outflows and may be a dominant source of cloud heating in molecular cloud cores. This view is controversial, but can be tested with observations as outlined below.

Although the statistics are still crude, young stars clearly accrete much of a stellar mass in FUor events. A typical eruption adds $\sim$ 0.01 M$_\odot$ to the central star; a rate of 10–20 eruptions per pre-main sequence star leads to a total accreted mass of $\sim$ 0.1–0.2 M$_\odot$. These eruptions eject considerable amounts of mass and momentum into the surrounding cloud. For example, FU Ori itself has lost material with a momentum of $\sim$ 0.3 M$_\odot$ km s^{-1} since its eruption began. With 10–20 such eruptions, FU Ori could supply a small fraction of the momentum of a typical molecular outflow, $(Mv)_o \sim$ 1–100 M$_\odot$ km s^{-1} ([45]).

Two conditions must be satisfied for a young star to accrete *all* of its mass in FUor events: 1. The disk must undergo regular thermal instabilities

and cycle between the low and high states on a reasonable time scale. 2. FUors must be young, $\lesssim$ a few $\times\ 10^5$ yr, to allow the surrounding cloud to fuel the recurring instabilities.

As a group, FUors clearly are young objects. FUors have many more properties in common with young class I protostars than older optically visible T Tauri stars. FUors have distinctive reflection nebulae and large far-IR excesses; most are associated with jets, HH objects, and molecular outflows. These properties are common in class I sources and rare in T Tauri stars ([145], [147], [49]). The typical age of a FUor is therefore $\sim$ a few $\times\ 10^5$ yr ([85], [184], [84]).

The conditions needed for the disk to cycle between the high and low states are probably satisfied in many pre-main sequence stars. For a typical infall rate of 1–10 $\times\ 10^{-6}$ $M_\odot\,\mathrm{yr}^{-1}$, theoretical models indicate that the disk spends most of its time in a low state where the mass accretion rate through the disk is much lower than the infall rate ([14], [15], [111]). The disk requires only $\sim 10^3$–10^4 yr to accumulate the ~ 0.01 $M_\odot$ needed to power a FUor eruption. The disk will continue to cycle between the low and high states as long as the cloud supplies mass to the disk.

If young stars accrete most of their mass in FUor events, it follows that FUors can power molecular outflows. In most outflow models, the mass ejected by the central star is $\sim 10\%$–30% of the accreted mass. For a wind velocity of ~ 200 km s^{-1}, the momentum in the wind is

$$(Mv)_w\ \sim\ 20\ (M_\star/M_\odot)\ M_\odot\ \mathrm{km\ s}^{-1} \tag{20}$$

for a typical wind velocity of 200 km s^{-1}. The observed range of outflow momenta $-\ (Mv)_o = 1$–100 $M_\odot$ km s^{-1} ([45]) – requires stellar masses of $M_\star \sim 0.1$–5 $M_\odot$ if the flows conserve momentum. The winds of FUors can power this outflow **if** a young star accretes most of its mass in FUor events.

These simple estimates establish that FUors are important events if they recur on time scales of $\sim 10^3$ yr during the protostellar phase of pre-main sequence stellar evolution. In this picture, the fraction of time in the FUor state is simply the ratio of the infall rate to the FUor accretion rate: $f \sim \dot{M}_i/\dot{M}_{FU}$. FUor disk models require $\dot{M}_{FU} \sim 10^{-4}$ $M_\odot\,\mathrm{yr}^{-1}$, so $f \sim 0.05$ for a typical infall rate of $\dot{M}_i \sim 5 \times 10^{-6}$ $M_\odot\,\mathrm{yr}^{-1}$. This prediction currently agrees with the statistics of FUors among protostars: 1 out of ~ 20 protostars in the Taurus dark cloud contains a FUor (L1551 IRS5; [85]) and 5 out of 17 protostars with HH objects contains a central star that resembles known FUors spectroscopically ([150]; see also [52]). Sensitive photometric and spectroscopic surveys of nearby molecular clouds can improve these statistics considerably. If the FUor frequency among protostars turns out to be more than a few per cent, then FUors may represent the main accretion phase of early stellar evolution.

References

1. Adams, F. C., Lada, C. J., & Shu, F. H. 1987, ApJ, 308, 788
2. Alves, J., Hartmann, L., Briceño, C., & Lada, C. J. 1997, AJ, 113, 1395
3. Ambartsumian, V. A. 1954, Comm. Byurakan Obs, No 13
4. Armitage, P. J. 1995, MNRAS, 274, 1242
5. Armitage, P. J. 1998, ApJL, 501, L189.
6. Bachiller, R., Tafalla, M., & Cernicharo, J. 1994, ApJo, 425, L93
7. Balbus, S. A., & Hawley, J. F. 1991, ApJ, 376, 214
8. Balbus, S. A., & Hawley, J. F. 1998, Rev Mod Phys, 70, 1
9. Balbus, S. A., Hawley, J. F., & Stone, J. M. 1996, ApJ, 467, 76
10. Baptista, R., Horne, K., Wade, R. A., Hubeny, I., Long, K. S., & Rutten, R. G. M. 1998, MNRAS, 298, 1079
11. Barth, W., Weigelt, H., & Zinnecker, H. 1994, A&A, 291, 500
12. Bastian, U., & Mundt, R. 1985, A&A, 144, 57
13. Bath, G.T., Evans, W.D., Papaloizou, J., & Pringle, J.E. 1974, MNRAS, 169, 447
14. Bell, K. R., & Lin, D. N. C. 1994, ApJ, 427, 987
15. Bell, K. R., Lin, D. N. C., Hartmann, L., & Kenyon, S. J. 1995, ApJ, 444, 376
16. Belyakina, T. S. 1992, Izv. Krym. Ap. Obs., 84, 45
17. Bertout, C., Bouvier, J., Duschl, W.J., & Tscharnuter, W.M. 1993, A&A, 275, 236
18. Bertout, C., & Regev, O. 1992, ApJ, 399, L163
19. Biscaya, A. M., Rieke, G. H., Narayanan, G., Luhman, K. L., & Young, E. T. 1997, AJ, 491, 359
20. Bonnell, I., & Bastian, P. 1992, ApJ, 401, L31
21. Bouvier, J., & Bertout, 1989, A&A, 211, 99
22. Bouvier, J., Cabrit, S., Fernandez, M., Martin, E. L., & Matthews, J. M. 1993, A&A, 272, 176
23. Bruch, A. 1994, in *Flares and Flashes*, IAU Colloquium No. 151, edited by J. Greiner, H. W. Duerbeck, & R. E. Gershberg, Berlin, Springer, p. 288
24. Cabot, W. 1996, ApJ, 465, 874
25. Cabot, W., Canuto, V. M., Hubickyj, O., & Pollack, J. B. 1987, Icarus, 69, 387
26. Calvet, N. & Gullbring, E. 1999, ApJ, in press
27. Calvet, N., Hartmann, L., & Kenyon, S. J. 1991, ApJ, 383, 752
28. Calvet, N., Hartmann, L., & Kenyon, S. J. 1993, ApJ, 402, 623
29. Campbell, C. G. 1987, MNRAS, 229, 405
30. Cannizzo, J. K., & Mattei, J. A. 1998, ApJ, 505, 344
31. Carr, J. S., Harvey, P. M., & Lester, D. F. 1987, ApJL, 321, L71
32. Clarke, C. J., Lin, D. N. C., & Papaloizou, J. C. B. 1989, MNRAS, 236, 495
33. Clarke, C. J., Lin, D. N. C., & Pringle, J. E. 1990, MNRAS, 242, 439
34. Clarke, C. J., & Syer, D. 1996, MNRAS, 278, L23
35. Cohen, M., Beiging, J. H., & Schwartz, P. R. 1982, ApJL, 289, L5
36. Cropper, M. 1990, Sp. Sci. Rev., 54, 195
37. Croswell, K., Hartmann, L., & Avrett, E. 1987, ApJ, 312, 227
38. Davis, C. J., Mundt, R., Eislöffel, J., & Ray, T. P. 1994, AJ, 110, 766
39. Eislöffel, J., Hessman, F. V., & Mundt, R. 1990, A&A, 232, 70
40. Elias, J. H. 1978, ApJ, 223, 859
41. Eislöffel, J., Günther, E., Hessman, F. V., Mundt, R., Carr, J. S., Beckwith, S., Ray, T. P. 1991, ApJ, 383, L19
42. Evans, II, N. J., Balkum, S., Levreault, R. M., Hartmann, L., & Kenyon, S. J. 1994, ApJ, 424, 793
43. Fridlund, C. V. M., Knee, L. B. G. 1993, A&A, 268, 245
44. Fridlund, C. V. M., & Liseau 1998, ApJ, 499, L75
45. Fukui, Y. 1989, in *ESO Workshop on Low Mass Star Formation and Pre-Main Sequence Objects,* edited by B. Reipurth, Garching, ESO, p. 95
46. Ghosh, P., & Lamb, F. K. 1979, ApJ, 232, 259

47. Godon, P., Regev, O., & Shaviv, G. 1995, MNRAS, 275, 1093
48. Godon, P. 1996, MNRAS, 279, 1071
49. Gómez, M., Whitney, B. A., & Kenyon, S. J. 1997, AJ, 114, 1138
50. Goodrich, R. 1987, PASP, 99, 116
51. Greene, T. P., & Lada, C. J. 1997, AJ, 114, 2157
52. Hanson, M. M., & Conti, P. S. 1995, ApJ, 448, L45
53. Hartigan, P., Raymond, J., & Meaburn, J. 1990, ApJ, 362, 624
54. Hartmann, L., & Calvet, N. 1995, AJ, 109, 1846
55. Hartmann, L., & Kenyon, S.J. 1985, ApJ, 299, 462
56. Hartmann, L., & Kenyon, S.J. 1987a, ApJ, 312, 243.
57. Hartmann, L., & Kenyon, S.J. 1987b, ApJ, 322, 393
58. Hartmann, L., Kenyon, S. J., Hewett, R., Edwards, S., Strom, K. M., Strom, S. E., & Stauffer, J. R. 1988, ApJ, 338, 1001
59. Hartmann, L., & Kenyon, S. J. 1996, ARA&A,
60. Hawley, J. F., & Balbus, S. A. 1991, ApJ, 376, 223
61. Herbig, G. H. 1960, ApJS, 4, 33
62. Herbig, G. H. 1966, Vistas in Astr, 8, 109
63. Herbig, G. H. 1977, ApJ,
64. Herbig, G. H. 1989, in *ESO Workshop on Low-Mass Star Formation and Pre-Main Sequence Objects* ed. B. Reipurth, Garching, ESO, p. 233
65. Herbig, G. H., & Petrov, P. P. 1992, ApJ, 392, 209
66. Herbst, W., *et al.* 1987, AJ, 94, 137
67. Herbst, W., Herbst, D. K., & Grossman, E. J. 1994, AJ, 108, 1906
68. Herrnstein, J. R., Greenhill, L. J., Moran, J. M., Diamond, P. J., Inque, M., Nakai, N., Miyoshi, M. 1998, ApJ, 497, L69
69. Hodapp, K.-W., Hora, J. L., Rayner, J. T., Pickles, A. J., & Ladd, E. F. 1996, ApJ, 468, 861
70. Horne, K., & Cook, M. C. 1985, MNRAS, 214, 307
71. Horne, K., & Steining, R. F. 1985, MNRAS, 216, 933
72. Hujeirat, A. 1995a, A&A, 295, 249
73. Hujeirat, A. 1995b, A&A, 295, 268
74. Ibragimov, M. A. 1993, Astr. Zh., 70, 339
75. Ibragimov, M. A. 1997, Pis'ma Astr. Zh., 1, 125
76. Idan, I. & Shaviv, G. 1996, MNRAS, 281, 604
77. Jayawardhana, R., Fisher, S., Hartmann, L., Telesco, C., Pina, R., & Fazio, G. 1998, ApJ:, 503, L79
78. Joy, A. H. 1945, ApJ, 102, 168
79. Kant, I. 1755, *Universal Natural History and Theories of the Heavens*
80. Kawazoe, E., & Mineshige, S. 1993, PASJ, 45, 715
81. Kenyon, S. J. 1986, *The Symbiotic Stars,* Cambridge University Press
82. Kenyon, S. J., Calvet, N., & Hartmann, L. 1993a, ApJ, 414, 676
83. Kenyon, S. J., & Hartmann, L. 1987, ApJ, 323, 714
84. Kenyon, S. J., & Hartmann, L. 1991, ApJ, 383, 664
85. Kenyon, S. J., & Hartmann, L. 1995, ApJS, 101, 117
86. Kenyon, S. J., Hartmann, L., Gómez, M., Carr, J., & Tokunaga, A. 1993b, AJ, 105, 1505
87. Kenyon, S. J., Hartmann, L., & Hewett, R. 1988, ApJ, 325, 231
88. Kenyon, S. J., *et al.* 1994, AJ, 107, 2153
89. Kenyon, S.J., Hartmann, L.W., Imhoff, C.L., & Cassatella, A. 1989, ApJ, 344, 925.
90. Kenyon, S. J., Hartmann, L., & Kolotilov, E. A. 1991, PASP, 103, 1069
91. Kenyon, S. J., & Webbink, R. F. 1984, ApJ, 279, 252
92. Kenyon, S. J., Whitney, B., Gómez, M., & Hartmann, L. 1993c, ApJ, 414, 773
93. Kenyon, S. J., Yi, I. & Hartmann, L. 1996, ApJ, 462, 439
94. Kholopov, P. N. 1959, Sov. AJ, 3, 291
95. Kley, W. 1991, A&A, 247, 95

96. Kley, W., & Hensler, G. 1987, A&A, 172, 124
97. Kley, W., & Lin, D. N. C. 1996, ApJ, 461, 933
98. Kley, W., & Papaloizou, J. C. B. 1997, MNRAS, 285, 239
99. Kolotilov, E. A., & Kenyon, S. J. 1998, IBVS, No. 4494
100. Kolotilov, E. A., & Petrov, P. P. 1983, Pis'ma Astr. Zh., 9, 171
101. Königl, A. 1991, ApJL, 370, L39
102. Koresko, C. D., Beckwith, S. V. W., Ghez, A. M., Matthews, K., Neugebauer, G. 1991, AJ, 102, 2073
103. Kuiper, G. P. 1941, ApJ, 93, 133
104. Lamzin, S. A. 1998, Astr. Rept., in press
105. Laplace, P. S. 1796, *Mécanique Céleste*
106. Larson, R. B. 1980, MNRAS, 190, 321
107. Li, J. 1996, ApJ, 456, 696
108. Liljeström, T., & Olofsson, G. 1997, ApJ, 478, 381
109. Lin, D. N. C., & Papaloizou, J. 1985, in *Protostars and Planets II,* ed. D. C. Black and M. S. Matthews, Tucson, University of Arizona Press, p. 981
110. Lin, D. N. C., & Papaloizou, J. C. B., 1996, ARA&A, 33, 505
111. Lin, D. N. C., & Papaloizou, J. C. B., 1996, ARA&A, 34, 703
112. Lin, D. N. C., & Pringle, J. E., 1987, MNRAS, 225, 607
113. Lipunov, V. M. 1978, Astron. Zh., 55, 1233
114. Lipunov, V. M. 1980, Astron. Zh., 57, 1253
115. Livio, M. 1997, in ASP Conf. Ser 121, *Accretion Phenomena and Related Outflows,* edited by D. T. Wickramasinghe, G. V. Bicknell, & L. Ferrario, San Francisco, ASP, p. 845
116. Looney, L. W., Mundy, L. G., & Welch, W. J. 1997, ApJ, 484, L157
117. López, R., *et al.* 1998, AJ, 116, 845
118. Lucas, P. W., & Roche, P. F. 1996, MNRAS, 280, 1219
119. Lüst, R. 1952, Zs. f. Nat., 7a, 87
120. Lynden-Bell, D., & Pringle, J. E. 1974, MNRAS, 168, 603
121. McMuldroch, S., Blake, G. A., & Sargent, A. I. 1995, AJ, 110, 354
122. Mahdavi, A., & Kenyon, S. J. 1998, ApJ, 497, 342
123. Malbet, F., *et al.* 1998, ApJL, 507, 149
124. Mardones, D., Myers, P. C., Tafalla, M., Wilner, D. J., Bachiller, R., & Garay, G. 1997, ApJ, 489, 719
125. Marsh, T. R., & Horne, K. 1988, MNRAS, 235, 269
126. Mould, J. R., Hall, D. N. B., Ridgway, S. T., Hintzen, P., & Aaronson, M. 1978, ApJL, 222, L123
127. Nakajima, T., & Golimowski, D. A. 1995, AJ, 109, 1181
128. Ohashi, N., Hayashi, M., Ho, P.T.P., Momose, M., & Hirano, N. 1996, ApJ, 466, 957
129. Okuda, T., Fujita, M., & Sakashita, S. 1997, PASJ, 49, 679
130. Oppenheimer, B. D., Kenyon, S. J., & Mattei, J. A. 1998, AJ, 115, 1175
131. Osaki, Y. 1974, PASJ, 26, 429
132. Papaloizou, J. C. B., & Stanley, G. Q. G. 1986, MNRAS, 220, 593
133. Petrov, P., Duemmler, R., Ilyin, I., Tuominen, I. 1998, A&A, 331, L53
134. Popham, R., & Narayan, R. 1991, ApJ, 370, 604
135. Popham, R., & Narayan, R. 1991, ApJ, 394, 255
136. Popham, R., Narayan, R., Hartmann, L., & Kenyon, S. J. 1993, ApJL, 415, L127
137. Popham, R., Narayan, R., Kenyon, S. J., & Hartmann, L. 1996, ApJ, 473, 422
138. Pringle, J. E. 1977, MNRAS, 178, 95
139. Pringle, J. E., Rees, M. J., & Pacholczyk, A. G. 1973, A&A, 29, 179
140. Pringle, J. E., & Savonije, G. J. 1979, MNRAS, 187, 777
141. Regev, O. 1983, A&A, 126, 146.
142. Regev, O., & Bertout, C. 1995, MNRAS, 272, 71
143. Regev, O., & Hougerat, A. A. 1988, MNRAS, 232, 81

144. Regös, E. 1997, MNRAS, 286, 104
145. Reipurth, B. 1985, A&A, 143, 435
146. Reipurth, B. 1989, Nature, 340, 42
147. Reipurth, B. 1990, in *Flare Stars in Star Clusters, Associations, and the Solar Vicinity,* IAU Symposium No. 137, Dordrecht, Kluwer, p. 229
148. Reipurth, B. 1991, in *Physics of Star Formation and Early Stellar Evolution,* NATO Adv. Study Inst., edited by C. J. Lada and N. D. Kylafis, p. 497
149. Reipurth, B. 1997, in *Low Mass Star Formation – from Infall to Outflow,* Poster Proceedings of IAU Symposium No. 182 on Herbig-Haro Objects and the Birth of Low Mass Stars, edited by F. Malbet & A. Castets, p. 309
150. Reipurth, B., & Aspin, C. 1997, AJ, 114, 2700
151. Reipurth, B., Bally, J., & Devine, D. 1997, AJ, 114, 2708
152. Reipurth, B., & Heathcote, S. 1992, A&A, 257, 693
153. Reipurth, B., Olberg, M., Gredel, R., & Booth, R. S. 1997, A&A, 327, 1164
154. Rodriguez, L., Hartmann, L. W., & Chavira, E. 1990, PASP, 102, 1413
155. Rodriguez, L., & Hartmann, L. 1992, Rev. Mex. A&A, 24, 135
156. Rodriguez, L., D'Alessio, P., Wilner, D.J., Ho, P.T.P., Torrelles, J.M., Curiel, S., Gómez, Y., Lizano, S., Pedlar, A., Canto, J., & Raga, A.C. 1998, Nat, 395, 355
157. Rozyczka, M., Bodenheimer, P., & Lin, D. N. C. 1996, ApJ, 459, 371
158. Rucinski, S. M. 1985, AJ, 90, 2321
159. Sandell, G., & aspin, C. 1998, A&A, 333, 1016
160. Sato, S., Okita, K., Yayamshita, T., Mizutani, K., Shiba, H., Kobayashi, Y., & Takami, H. 1992, ApJ, 398, 273
161. Shakura, N. I., & Sunyaev, R. A. 1973, A&A, 24, 337
162. Shevchenko, V. S. 1995, rotor project
163. Shevchenko, V. S., Ezhkova, O., Tjin A Djie, H. R. E., van den Anckner, M. E., Blondel, P. F. C., & de Winter, D. 1997, A&AS, 124, 33
164. Smith, B. A., & Terrile, R. J. 1984, Science, 226, 1421
165. Staude, H. J., & Neckel, Th. 1991, A&A, 244, L13
166. Staude, H. J., & Neckel, Th. 1992, ApJ, 400, 556
167. Stocke, J. T., Hartigan, P. M., Strom, S. E., Strom, K. M., Anderson, E. R., Hartmann, L. W., & Kenyon, S. J. 1988, ApJS, 68, 229
168. Stone, J. M. & Balbus, S. A. 1996, ApJ, 464, 364
169. Strom, K. M., & Strom, S. E. 1993, ApJL, 421, L63
170. Teodorani, M., Errico, L., Vittone, A. A., Giovanelli, F., & Rossi, C. 1997, A&AS, 126, 91
171. Thiebaut, E., Bouvier, J., Blazit, A., Bonneau, D., Foy, F.-C. & Foy, R. 1995, A&A, 303, 795
172. Tout, C. A., & Pringle, J. E. 1992, MNRAS, 259, 604
173. Turner, N. J. J., Bodenheimer, P., & Bell, K. R. 1997, ApJ, 480, 754
174. Tylenda, R. 1981, Acta Astr., 31, 267
175. Ulrich, M.-H., Maraschi, L., & Urry, C. M. 1997, ARA&A, 35, 445
176. Vishniac, E. T., & Diamond, P. 1989, ApJ, 347, 435
177. Vishniac, E. T., & Zhang, C. 1996, ApJ, 461, 307
178. von Weiszäcker, C. F. 1943, Zs. f. Ap., 22, 319
179. von Weiszäcker, C. F. 1948, Zs. f. Nat., 3a, 524
180. Wachman, A. A. 1939, Beob. Zirk., 21, 60
181. Wachman, A. A. 1954, Zs. f. Ap., 35, 74
182. Wang, Y. M. 1997, ApJL, 475, 135
183. Weintraub, D. A., Sandell, G., & Duncan, W. D. 1989, ApJ, 340, 69
184. Weintraub, D. A., Sandell, G., & Duncan, W. D. 1991, ApJ, 382, 270
185. Welin, G. 1971, A&A, 12, 312
186. Welty, A. D., Strom, S. E., Strom, K. M., Hartmann, L., Kenyon, S. J., Grasdalen, G. L., & Stauffer, J. R. 1991, ApJ, 349, 328
187. Welty, A. D., Strom, S. E., Edwards, S., Kenyon, S. J., & Hartmann, L. W. 1992,

ApJ, 397, 260
188. Whitney, B. A., Clayton, G. C., Schulte-Ladbeck, R. E., Calvet, N., Hartmann, L. & Kenyon, S. J. 1993, ApJ, 417, 687
189. Yamashita, T., & Tamura, M. 1992, ApJL, 387, L93
190. Yang, J., Ohashi, N., & Fukui, Y. 1995, ApJ, 455, 175
191. Yi, I. 1994, ApJ, 428, 760
192. Yun, J. L., Moreira, M. C., Alves, J. F., & Storm, J. 1997, A&A, 320, 167